Applied Mathematical Modelling 40 (2016) 451–467

Contents lists available at ScienceDirect

Applied Mathematical Modelling

journal homepage: www.elsevier.com/locate/apm

Non-linear dynamic response to simple harmonic excitation of a thin-walled beam with a breathing crack

Franco E. Dotti, Víctor H. Cortínez *, Florencia Reguera

Centro de Investigaciones en Mecánica Teórica y Aplicada, Universidad Tecnológica Nacional, FRBB, 11 de Abril 461, B8000LMI Bahía Blanca, Argentina
Consejo Nacional de Investigaciones Científicas y Técnicas, CONICET, Argentina

ARTICLE INFO

Article history:
Received 21 January 2014
Received in revised form 11 February 2015
Accepted 22 April 2015
Available online 9 June 2015

Keywords:
Thin-walled beams
Breathing crack
Period doubling
Quasi-periodicity

ABSTRACT

The dynamic response of a thin-walled beam with a breathing crack is studied by employing a refined one-dimensional model introduced for such purpose. It is shown that, due to the non-linearity of breathing, some effects take place which are impossible by using a completely open crack model. Even with the simplest of sinusoidal excitations, the system under study reveals a rich and complex dynamics. Some of the topics emphasized in the article are self-excitation of harmonic resonances, period doubling and the presence of quasi-periodic motion. Furthermore, the possibility of chaotic vibrations is analyzed.

1. Introduction

The presence of damage represents a crucial topic regarding safety of engineering structures. Since early damage detection may prevent the possibility of service failures, the development of structural health monitoring techniques has acquired a remarkable importance in recent years [1–3]. A very common damage typology that appears in dynamic operating condition corresponds to fatigue cracks. These cracks are usually invisible to the naked eye and their identification by local non-destructive methods, such as dye penetrant and ultrasonic testing, may be impractical if the structure must remain in service.

These aspects lead to the need of mathematical models as interpretative tools for crack identification, which is generally performed by solving an inverse optimization problem [4]. This problem is usually complex from a mathematical point of view, and also must be solved quickly. Hence models must combine precision and simplicity in balanced form. For slender structures, a beam model captures the most significant features of the structural dynamics. And at the same time it is simple enough for extensive computational treatment, an essentially useful feature when damage diagnosis must be performed in real time. Most studies have focused on Bernoulli–Euler beams [5–9] and, to a lesser extent, on Timoshenko beams [10–13]. Thin-walled beams have not been addressed in depth, perhaps due to their more complex dynamics, usually presenting a strongly coupled vibrational response [14–22].

Crack models are generally assumed to be linear, with a crack remaining open during vibration. But while this hypothesis works well for many situations, it is more realistic to consider a fatigue crack which may be open or closed during the motion [10,23,24]. This "breathing effect" introduces a non-linearity in the system since the stiffness of the structure becomes time

* Corresponding author at: Centro de Investigaciones en Mecánica Teórica y Aplicada, Universidad Tecnológica Nacional, FRBB, 11 de Abril 461, B8000LMI Bahía Blanca, Argentina. Tel.: +54 291 4555220; fax: +54 291 4555311.
E-mail address: vcortine@frbb.utn.edu.ar (V.H. Cortínez).

http://dx.doi.org/10.1016/j.apm.2015.04.052
0307-904X/

Nomenclature

A	crack depth (also semi-major axis of the elliptic crack)
$\tilde{a}$	variable crack depth
A	cross-sectional area
A_f	loading amplitude
b	dimension of a flange
B	bimomental beam force (also point B, origin of the system B: x, s, n)
c	semi-minor axis of the elliptic crack
C	center of gravity of the uncracked cross section
C_w	warping constant
$\mathbf{D}$	damping matrix
E	Young's modulus
f	driving frequency, expressed in Hz
f_B	bilinear frequency, expressed in Hz
$\mathbf{F}_C^{(e)}$	flexibility matrix of the cracked element
G	shear modulus
G^*	crack mouth widening energy release rate
h	dimension of the web
H	point placed at the cracked branch of the cross-section
I_y, I_z	second moments of area
I_{yz}	product moment of area
$I_{y\omega}$, $I_{z\omega}$	product of warping
I_{sv}	Saint–Venant's torsion constant
I_{ij}	shear coefficients of the constitutive matrix
J	Rice's J integral
$\mathbf{J}$	constitutive matrix of the beam
K	point placed at the cracked branch of the cross-section
$\mathbf{K}_0$	global stiffness matrix of an intact beam
$\mathbf{K}_C$	global stiffness matrix of a beam with a fully open crack
$\mathbf{K}_B$	global stiffness matrix of a beam with a breathing crack
$\mathbf{K}_C^{(e)}$	stiffness matrix of the cracked element
L	length of the beam
M_x	total torque
$\mathbf{M}$	inertia matrix of the uncracked beam
n	coordinate normal to the cross-section middle line
N	axial beam force
M_y, M_z	bending moments
$\mathbf{p}^{(i)}$	vector of nodal forces of node i
P_i	nodal forces
$\mathbf{Q}$	vector of generalized forces
r	distance in s-direction from C to a point in the cross-section middle line
s	circumferential coordinate
S	cross-sectional perimeter
S_y, S_z	first moments of area
S_ω	first moment of warping
t	wall thickness
T_f	driving period
$\mathbf{T}$	transformation matrix
T_{sv}	Saint–Venant torque
T_w	Vlasov torque
u, v, w	displacements of the uncracked beam centroid
u_x, u_y, u_z	displacements of any point of the beam
U	strain energy of the beam
U_0	strain energy of the uncracked element
U_C	strain energy due to the presence of a crack
V	work of external loads
$\mathbf{w}^{(i)}$	vector of nodal displacements of node i
x, y, z	Cartesian coordinates
$\bar{x}_C$	location of the crack in the cracked element
Y, Z	coordinates of a point located in the middle line of the cross-section

α	damping proportionality factor
β	damping proportionality factor
$\mathbf{\Lambda}$	vector of generalized strains
Δu_{HK}	crack breathing index
θ_x	warping variable
θ_y, θ_z	bending twists
λ	auxiliary integration variable
ξ	crack location (axial coordinate of the crack)
Π	total potential energy
ϖ	driving frequency, expressed in s^{-1}
ϖ_B	bilinear frequency, expressed in s^{-1}
ω_p	primary warping function associated to the uncracked cross-section
τ_0	time constant arbitrarily chosen to improve visualization of Poincaré maps
ζ	damping ratio
$(\bullet)_0$	subscript associated to the uncracked cross-section
$(\bullet)_{\tilde{a}}$	subscript associated to the cracked cross-section (with x as integration variable)
$(\bullet)_\lambda$	subscript associated to the cracked cross-section (with λ as integration variable)
${}^t(\bullet)$	superscript denoting time dependence

dependent. The most extended approach is the use of a bilinear model, i.e. a piecewise linear stiffness, combining the open crack case and the uncracked case [24,25]. The exchange strategy is based on checking the status (open or closed) of the crack, using different control variables such as natural frequencies [26], structural damping [27], bending rotations [28–30], displacements [21], excitation frequency (only for low frequencies) [10,31] or shaft periodicity (only in the case of rotors) [32–34]. More sophisticated models have treated breathing as a contact problem [35–37]. These approaches are probably more realistic, but they can also be impractical for crack detection since the computation time is often prohibitive, especially in relatively complex structures such as thin-walled beams. Furthermore, experimental tests could be needed in order to validate numerical methods devoted to the identification of breathing cracks [38].

This article aims to give a picture of the non-linear dynamics of thin-walled beams with breathing cracks. For such purpose, a finite element is introduced as an extension of the one-dimensional formulation originally proposed in Ref. [16] for intact beams. This is an element with two nodes and seven degrees-of-freedom per node, and accounts for shear flexibility due to bending and warping. The breathing effect is modeled as a bilinear stiffness, employing the relative axial displacements of the cracked element as closure index. Implementation is performed during the integration of the equations of motion, through a simple adaptation of the Newmark scheme for linear systems. Using a sinusoidal excitation and taking the driving frequency as a parameter, time history responses are obtained to search for topological changes in the vibration motion. Since the system under study has similarities with a bilinear oscillator, these changes should be associated with the excitation of multiples and sub-multiples of the bilinear resonances. By using tools of non-linear dynamics as bifurcation diagrams and Poincaré maps [39], we study the possibility of period doubling, quasi-periodicity and chaotic motion in the phase plane.

2. Beam model

2.1. A cracked thin-walled beam

Fig. 1 shows a sketch of a generic thin-walled beam with an edge crack. The points of the beam are referred to a Cartesian coordinate system (C: x, y, z), which origin C is located at the centroid of the uncracked cross-section. An intrinsic coordinate system (B: x, s, n) is also defined, which origin B is over the middle line of the cross-section. The coordinates of a generic point on this middle line are $Y(s)$ and $Z(s)$.

A crack with depth a and location $x = \xi$ is regarded as an elliptical hole (see Fig. 1). The condition $c \to 0$ [40–42] is strictly necessary for the hole to actually represent a crack (with a finite value of c, it would be an elliptical notch, but not a crack). The crack boundary can be expressed as

$$\tilde{a}(x) = a\sqrt{1 - \frac{(x-\xi)^2}{c^2}}, \tag{1}$$

where $\tilde{a}(x)$ describes a variable cross section in the cracked zone. One can see that if c approaches to zero, then $\tilde{a}(x)$ approaches to a, and therefore the infinitesimal nature of the crack is obtained.

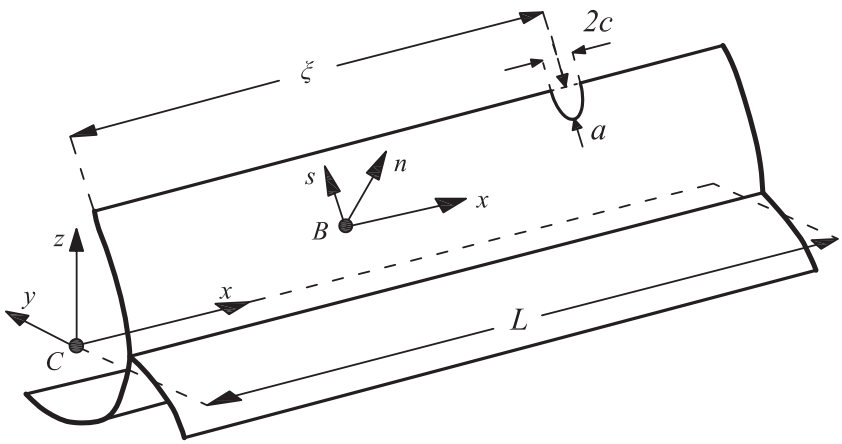

Fig. 1. Generic thin-walled beam with an edge crack regarded as an elliptical hole ($c \to 0$).

2.2. Constitutive law

The constitutive equation for a thin-walled beam can be written as [17]

$$\mathbf{Q} = \mathbf{J}\boldsymbol{\Delta}, \tag{2}$$

where $\mathbf{Q}$ is the vector of generalized beam forces, $\mathbf{J}$ the constitutive matrix and $\boldsymbol{\Delta}$ the vector of generalized strains. These are given by

$$\mathbf{Q} = \{N, M_y, M_z, B, Q_y, Q_z, T_w, T_{sv}\}^T, \tag{3}$$

$$\boldsymbol{\Delta} = \left\{\frac{\partial u}{\partial x}, -\frac{\partial \theta_y}{\partial x}, -\frac{\partial \theta_z}{\partial x}, -\frac{\partial \theta_x}{\partial x}, \frac{\partial v}{\partial x} - \theta_z, \frac{\partial w}{\partial x} - \theta_y, \frac{\partial \phi_x}{\partial x} - \theta_x, \frac{\partial \phi_x}{\partial x}\right\}^T. \tag{4}$$

The following generalized beam forces defined in Eq. (3) are: the axial force N, the bending moments M_y and M_z, the bimoment B, the shear forces Q_y and Q_z, the Vlasov torque T_w and the Saint–Venant torque T_{sv}. The generalized strains in vector $\boldsymbol{\Delta}$ are defined in terms of the generalized displacements: u is the axial displacement, v and w are the displacements in directions y and z, respectively, θ_y and θ_z are the bending rotations, θ_x is the warping variable and ϕ_x is the torsional twist. The constitutive matrix $\mathbf{J}$ is given by

$$\mathbf{J} = \begin{bmatrix} EA & ES_y & ES_z & ES_\omega & 0 & 0 & 0 & 0 \\ & EI_y & EI_{yz} & EI_{y\omega} & 0 & 0 & 0 & 0 \\ & & EI_z & EI_{z\omega} & 0 & 0 & 0 & 0 \\ & & & EC_w & 0 & 0 & 0 & 0 \\ & & & & GI_{55} & 0 & GI_{57} & 0 \\ & & & & & GI_{66} & GI_{67} & 0 \\ & & & & & & GI_{77} & 0 \\ & & & & & & & GI_{sv} \end{bmatrix}, \tag{5}$$

where I_{sv} is the Saint–Venant's torsion constant. In Eq. (5) the following cross-sectional magnitudes have been defined

$$\begin{aligned} &A = t\int_S ds, \quad S_y = t\int_S Z ds, \quad S_z = t\int_S Y ds, \quad S_\omega = t\int_S \omega_p ds, \\ &I_y = t\int_S Z^2 ds, \quad I_z = t\int_S Y^2 ds, \quad I_{yz} = t\int_S YZ ds, \\ &I_{y\omega} = t\int_S Z\omega_p ds, \quad I_{z\omega} = t\int_S Y\omega_p ds, \quad C_w = t\int_S \omega_p^2 ds, \end{aligned} \tag{6}$$

and the shear coefficients [15–17], given by

$$\begin{aligned} &I_{55} = t\int_S \left[\left(\frac{dY}{dS}\right)^2 + \left(\frac{dZ}{dS}\right)^2\right] ds, \quad I_{66} = t\int_S \left[\left(\frac{dY}{dS}\right)^2 + \left(\frac{dZ}{dS}\right)^2\right] ds, \quad I_{77} = t\int_S r^2 ds, \\ &I_{57} = t\int_S \left[r\left(\frac{dY}{dS}\right)^2\right] ds, \quad I_{67} = t\int_S \left[r\left(\frac{dZ}{dS}\right)^2\right] ds, \end{aligned} \tag{7}$$

where t is the wall thickness, ω_p is the primary warping function [17] and $r = -ZdY/ds + YdZ/ds$. S denotes the contour perimeter of the cross-section. It becomes S_0, constant, if reference is made to the intact cross-section or $S_{\bar{a}}$, dependent on x, if the cross-section contains the elliptical crack.

2.3. Energy release rate due to widening of crack mouth

The strain energy related to the generic beam in Fig. 1 can be expressed as

$$U = \frac{1}{2}\left(\int_0^{\xi-c} \mathbf{Q}^T\mathbf{J}_0^{-1}\mathbf{Q}dx + \int_{\xi-c}^{\xi+c} \mathbf{Q}^T\mathbf{J}_{\bar{a}}^{-1}\mathbf{Q}dx + \int_{\xi+c}^{L} \mathbf{Q}^T\mathbf{J}_0^{-1}\mathbf{Q}dx\right), \tag{8}$$

where $\mathbf{J}_{\bar{a}}$ and $\mathbf{J}_0$ are the constitutive matrices associated to the cracked and uncracked cross-section, respectively. $\mathbf{J}_{\bar{a}}$ depends on x through Eq. (1). Then, neglecting the small alterations generated in the beam forces by the presence of the crack, Eq. (8) can be reformulated as

$$U = \frac{1}{2}\left(\int_0^{\xi-c} \mathbf{Q}^T\mathbf{J}_0^{-1}\mathbf{Q}dx + c\mathbf{Q}^T\Big|_{x=\xi}\int_{-1}^{1}\mathbf{J}_\lambda^{-1}d\lambda\mathbf{Q}|_{x=\xi} + \int_{\xi+c}^{L} \mathbf{Q}^T\mathbf{J}_0^{-1}\mathbf{Q}dx\right), \tag{9}$$

where an additional integration variable $\lambda = (x-\xi)/c$ has been defined.

From Clapeyron's theorem, the work of external loads is $V = 2U$. The potential energy is given by $\Pi = U - V$, therefore $\Pi = -U$. Then the crack surface widening energy release rate [40–44] can be expressed as

$$G^* = \lim_{c\to 0}\frac{\partial U}{\partial c} = \frac{1}{2}\frac{\partial}{\partial c}\left(\int_0^{\xi-c} \mathbf{Q}^T\mathbf{J}_0^{-1}\mathbf{Q}\,dx + \int_{\xi+c}^{L} \mathbf{Q}^T\mathbf{J}_0^{-1}\mathbf{Q}\,dx\right) + \mathbf{Q}^T|_{x=\xi}\int_0^1 \mathbf{J}_\lambda^{-1}d\lambda\mathbf{Q}|_{x=\xi}. \tag{10}$$

This expression can be rearranged by applying the fundamental theorem of calculus to give

$$G^* = \mathbf{Q}^T|_{x=\xi}\left(\int_0^1 \mathbf{J}_\lambda^{-1}d\lambda - \mathbf{J}_0^{-1}\right)\mathbf{Q}|_{x=\xi}. \tag{11}$$

3. Numerical implementation

3.1. Cracked finite element

Consider a generic thin-walled beam segment containing a crack at one of its branches at $x = \bar{x}_C$, as shown in Fig. 2. This segment is represented by a beam element with two nodes, N_1 and N_2, and seven degrees of freedom per node, similarly as the original element for intact beams [16]. Nevertheless, the stiffness matrix must be different from that corresponding to an intact element, since it must take into account the coupling phenomena due to the presence of the crack. This element with modified stiffness matrix is then introduced into a conventional finite element assembly, which is used in subsequent analyses.

The cracked element stiffness matrix is obtained similarly as proposed in Ref. [32] for rotors, but considering specific aspects of thin-walled beams. The element, of length L_C, is loaded with axial forces P_1 and P_8, shear forces P_2, P_4 and P_9, P_{11}, bending moments P_3, P_5 and P_{10}, P_{12}, torques P_6 and P_{13}, and bimomental forces P_7 and P_{14}. The crack is located at a distance $\bar{x}_C$ from node N_1. From Castigliano's theorem, the displacements of node N_1 can be expressed as follows

$$\mathbf{w}^{(1)} = \frac{\partial(U_0 + U_C)}{\partial \mathbf{p}^{(1)}}, \tag{12}$$

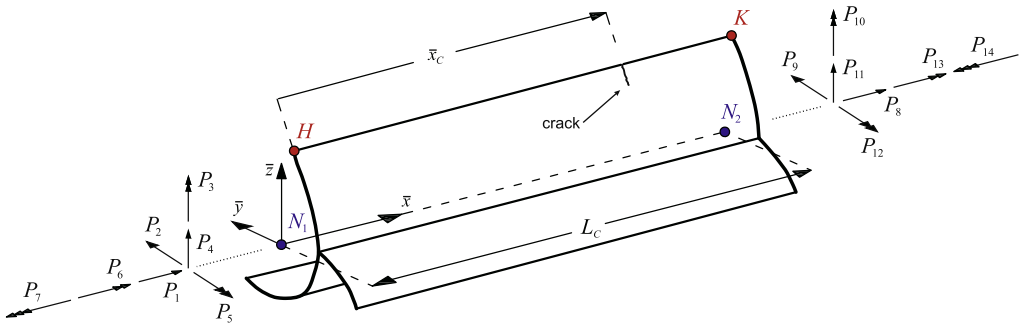

Fig. 2. Generic thin-walled cracked beam element with applied nodal forces and local coordinate system.

where U_0 is the strain energy of the uncracked element and U_C is the strain energy due to the presence of the crack. In Eq. (12), displacement and force vectors have been defined respectively for the node N_1 as

$$\mathbf{w}^{(1)} = \left\{u^{(1)}, v^{(1)}, \theta_z^{(1)}, w^{(1)}, \theta_y^{(1)}, \phi_x^{(1)}, \theta_x^{(1)}\right\}^T, \tag{13}$$

and

$$\mathbf{p}^{(1)} = \{P_1, P_2, P_3, P_4, P_5, P_6, P_7\}^T. \tag{14}$$

Nodal forces can be expressed in terms of generalized beam forces. From Fig. 2 one can obtain

$$\begin{aligned} &N = P_1, \quad Q_y = P_2, \quad M_z = P_3 - \bar{x}_C P_2, \quad Q_z = P_4, \\ &M_y = P_5 - \bar{x}_C P_4, \quad T_{sv} = P_{6a}, \quad T_w = P_{6b}, \quad B = P_7 - \bar{x}_C P_{6b}, \end{aligned} \tag{15}$$

where $P_6 = P_{6a} + P_{6b}$ since the total torque is given by $M_x = T_{sv} + T_w$ [13,14].

The strain energy due to the crack can be derived from concepts of fracture mechanics [45,46] by considering the relation $J = \pi G^*$ and Eq. (12). That is

$$U_C = \int_0^a J da = \pi \int_0^a G^* da = \pi \mathbf{Q}^T|_{x=\xi} \left(\int_0^a \int_0^1 \mathbf{J}_\lambda^{-1} d\lambda da - a\mathbf{J}_0^{-1} \right) \mathbf{Q}|_{x=\xi}. \tag{16}$$

Now, employing Eqs. (12) and (15), and taking into account that U_0 is given by

$$U_0 = \frac{1}{2} \int_0^{L_C} \mathbf{Q}^T \mathbf{J}_0^{-1} \mathbf{Q} dx, \tag{17}$$

the vector of nodal displacements can be expressed in terms of the vector of nodal forces as

$$\mathbf{w}^{(1)} = \mathbf{F}_C^{(e)} \mathbf{p}^{(1)}, \tag{18}$$

where $\mathbf{F}_C^{(e)}$ is the flexibility matrix of the cracked element. Since static equilibrium must be fulfilled within the element, the stiffness matrix can be obtained as [32]

$$\mathbf{K}_C^{(e)} = \mathbf{T}^T \left(\mathbf{F}_C^{(e)} \right)^{-1} \mathbf{T}, \tag{19}$$

where a transformation matrix $\mathbf{T}$ has been defined as

$$\mathbf{T} = \begin{bmatrix} 1 & 0 & 0 & 0 & 0 & 0 & 0 & 0 & -1 & 0 & 0 & 0 & 0 & 0 & 0 & 0 \\ 0 & 1 & 0 & 0 & 0 & 0 & 0 & 0 & 0 & -1 & L_C & 0 & 0 & 0 & 0 & 0 \\ 0 & 0 & 1 & 0 & 0 & 0 & 0 & 0 & 0 & 0 & -1 & 0 & 0 & 0 & 0 & 0 \\ 0 & 0 & 0 & 1 & 0 & 0 & 0 & 0 & 0 & 0 & 0 & -1 & L_C & 0 & 0 & 0 \\ 0 & 0 & 0 & 0 & 1 & 0 & 0 & 0 & 0 & 0 & 0 & 0 & -1 & 0 & 0 & 0 \\ 0 & 0 & 0 & 0 & 0 & 1 & 0 & 0 & 0 & 0 & 0 & 0 & 0 & -1 & 0 & 0 \\ 0 & 0 & 0 & 0 & 0 & 0 & 1 & 0 & 0 & 0 & 0 & 0 & 0 & 0 & -1 & L_C \\ 0 & 0 & 0 & 0 & 0 & 0 & 0 & 1 & 0 & 0 & 0 & 0 & 0 & 0 & 0 & -1 \end{bmatrix}. \tag{20}$$

In order to properly use the stiffness matrix $\mathbf{K}_C^{(e)}$ into the conventional finite element assembly, columns and rows associated with P_{6a} and P_{6b} must be condensed.

3.2. Breathing effect

The presence of a breathing crack causes the global stiffness matrix to be time dependent. In a similar manner as it has been considered in previous models [24], breathing is simulated with a bilinear stiffness scheme. Thus, the stiffness is piecewise constant and the global stiffness matrix is obtained by conveniently exchanging the one associated to the intact beam ($\mathbf{K}_0$) with the one obtained by considering a fully open crack ($\mathbf{K}_C$). Therefore, the global stiffness matrix of the beam with a breathing crack is expressed as

$$\mathbf{K}_B = \begin{cases} \mathbf{K}_0 & \text{if} \quad {}^t\Delta u_{HK} < 0 \\ \mathbf{K}_C & \text{if} \quad {}^t\Delta u_{HK} \geqslant 0 \end{cases}. \tag{21}$$

The crack is assumed to be closed if the breathing index ${}^t\Delta u_{HK}$ is negative, and open if it is positive. The index ${}^t\Delta u_{HK}$ is given by the difference among the axial displacements of the points H and K, shown in Fig. 2. That is

$${}^t\Delta u_{HK} = {}^t u_x^{(K)} - {}^t u_x^{(H)}. \tag{22}$$

Displacements ${}^t u_x^{(H)}$ and ${}^t u_x^{(K)}$ are obtained from the displacement field of the beam model [16], having the following expressions

$$ {}^t u_x^{(H)} = {}^t u(x_H) - y_H {}^t\theta_z(x_H) - z_K {}^t\theta_y(x_H) - \omega {}^t\theta_x(x_H), \tag{23} $$

$$ {}^t u_x^{(K)} = {}^t u(x_K) - y_K {}^t\theta_z(x_K) - z_K {}^t\theta_y(x_K) - \omega {}^t\theta_x(x_K), \tag{24} $$

where $\{x_H = \xi - \bar{x}_C, y_H, z_H\}$ and $\{x_K = \xi + L_C - \bar{x}_C, y_K, z_K\}$ are the coordinates of the points H and K respectively. The superscript t on the left of the displacement magnitudes denotes time dependence.

The bilinear model represented by Eq. (21) preserves the properties of two linear models: fully open crack and intact beam. All the nonlinear features of the model are derived from the crack breathing mechanism. This form of considering breathing is easily adaptable to a finite element model, capturing the main source of nonlinearity of a fatigue crack at a relatively low computational cost.

3.3. Damping

The damping matrix $\mathbf{D}$ is assumed to be proportional to a combination of the mass and the stiffness matrices corresponding to the case of the intact beam, namely

$$ \mathbf{D} = \alpha \mathbf{M} + \beta \mathbf{K}_0, \tag{25} $$

where α and β are proportionality factors which can be evaluated if the damping ratios associated with two specific modes are known [46]. Because detailed information about the variation of damping ratio with frequency is not available, we assume that the same damping ratio, ζ, applies to two control frequencies: the fundamental frequency, ϖ_1, and the higher frequency which contributes significantly to the dynamic response, ϖ_n. Thus, α and β are calculated approximately by using the following formula given by Clough and Penzien [46]

$$ \begin{Bmatrix} \alpha \\ \beta \end{Bmatrix} = \frac{2\zeta}{\varpi_1 + \varpi_n} \begin{Bmatrix} \varpi_1 \varpi_n \\ 1 \end{Bmatrix}. \tag{26} $$

Although this way of considering damping is very simple and usually employed [9,10], it is in fact a rough approximation. First of all, an important matter is missed: the presence of fatigue cracks cause an increase of damping. This increase is mainly due to the energy dissipated by elasto-plastic deformations in the vicinity of the crack tip and, in a lesser extent, to friction among the crack surfaces [47,48]. This energy dissipation is was shown to be proportional to the thickness [47,49], which is a small magnitude in thin-walled beams. Besides, in the range of stresses of interest in engineering, the increase of damping due to the crack must be studied regarding damping as a function of the amplitude of vibration.

The damping level of the system was found to have considerable influence on the harmonic resonances and bifurcation phenomena of cracked structures [33,50]. Therefore damping must be carefully determined before employing the present model as a tool for damage detection. Consequently, more experimental and analytical research is needed to quantify the increase of damping by the presence of a fatigue crack in thin-walled beams.

3.4. Note on the solution of the dynamic equilibrium equation

In a general case, the equation of forced vibrations of a beam with a breathing crack is non-linear [51]. But if the crack is small to moderate, the nonlinearity introduced by the breathing effect can be considered as weak since the percentage change in the components of the stiffness matrix is small [52]. Thus, instead of solving the nonlinear equation of motion, the linear equation can be solved considering this small variation of the stiffness [10]. The dynamic equilibrium equation is then solved using the classic Newmark implicit integration scheme for linear systems. Using this technique, a small error is introduced during the process of change of state of the crack (open to closed and *vice versa*). This is due to the imbalance between internal and external forces generated by the sudden change of the stiffness matrix. This error decreases to the point of being negligible if a relatively small time step is used in the integration, keeping the advantage of solving an almost entirely linear problem.

4. Numerical results and discussion

4.1. Overview

In this section, we examine the nonlinear vibratory behavior of a cracked thin-walled beam. Numerical calculations are performed for a cantilever beam with U-shaped cross-section, as shown in Fig. 3, with dimensions: $h = 0.2$ m, $b = 0.1$ m, $t = 0.01$ m and $L = 2$ m. We consider a crack located at one flange of the cross-section, which results in the coupling of flexural and torsional motion. Crack location and depth are $\xi/L = 0.1$ and $a/b = 0.5$ respectively. The beam is made of carbon steel with the following material properties: Young modulus $E = 210$ GPa, shear modulus $G = 80.76$ GPa, Poisson ratio $\nu = 0.3$ and mass density $\rho = 7830$ kg/m^3. Five frequencies are considered to contribute significantly to the dynamic response and ς is assumed

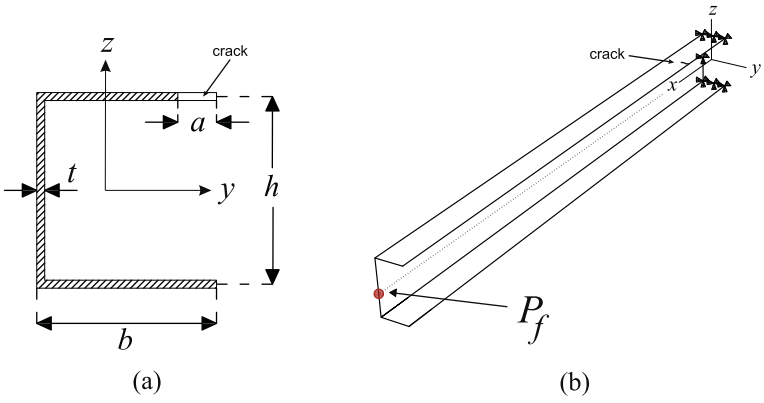

Fig. 3. (a) Cross sectional shape under study with its corresponding crack disposition. (b) Location of the point $P_f = \{L, -b^2/(2b+h), 0\}$ where displacements are measured.

to be 0.02, as in Ref. [9]. The free end of the beam is loaded with a shear sinusoidal force given by $Q_y(L) = 5000\,N \sin(\varpi t)$ and $f = \varpi/(2\pi)$ is defined in order to express the driving frequency in Hz. We arbitrarily chose the forcing amplitude ensuring that there is no evidence of geometric nonlinear response in the undamaged case. It is assumed that, within the loading history, the crack remains stable and no propagation takes place.

Newmark implementation is based on the procedure in Ref. [53], with a slight adaptation: at each time step, expression (21) is evaluated to determine the global stiffness matrix, without the need of iterations. The robustness of this numerical procedure is checked in all the performed analyses. Although time histories can be obtained with acceptable accuracy using 25 elements and 40 calculations per loading period, a total of 35 elements and 120 calculations are employed to obtain very accurate results in the phase plane and bifurcation diagram. Displacements, velocities and accelerations are observed at the point P_f, which is defined in Fig. 3.

4.2. Validation of the model

To validate the model, we compare time histories of motion with results obtained from a shell model, programmed in ABAQUS. This shell model is a higher hierarchy model, in which breathing effect is modeled as a contact problem. The crack is modeled as a couple of contact interfaces, with duplicated nodes. We consider edge-to-edge contact with the following conditions: *Hard contact* for normal interaction, which allows total transmission of pressure when the surfaces are in contact; after contact, separation is allowed, taking place if the contact pressure is reduced to zero. Tangential behavior is modeled with the *rough* friction formulation, which prevents sliding once contact has occurred [54]. This procedure is similar to that employed in Ref. [35,36] for Euler–Bernoulli beams. Time histories of the shell model are obtained with the ∗DYNAMIC procedure of ABAQUS/Explicit [55].

Fig. 4 shows a comparison among shell and beam models. A very good agreement can be noted for displacements u_x and u_y, i.e. axial displacement and displacement in the direction of the load, respectively. Some minor differences can be observed for the transversal displacement, u_z, but the results are also fairly good. Of course, it may be taken into account that in real physics, as has been pointed by Brandon and co-workers [28,56], there is no unique instant of closure. Indeed, it has been shown [57] that minor variations in the modeling of the crack transition (open to closed, and *vice versa*)

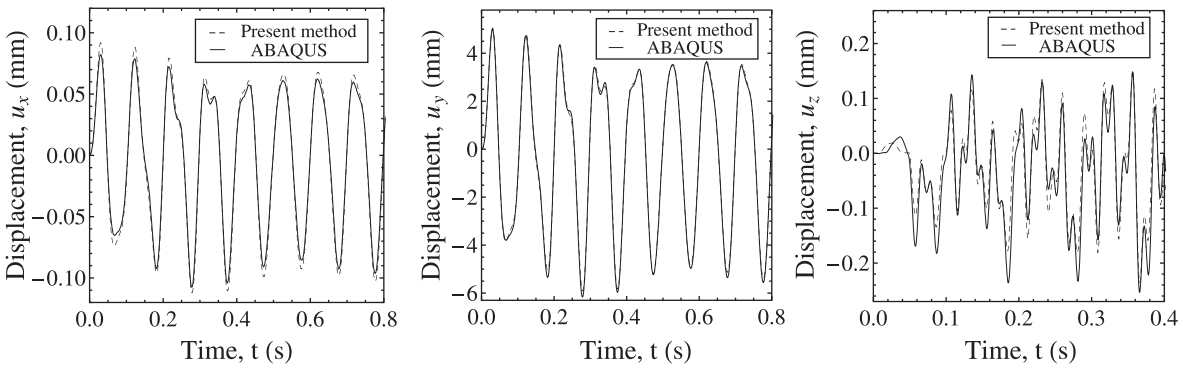

Fig. 4. Time history of displacements for the point P_f, comparison with ABAQUS. Excitation frequency: $f = 10$ Hz.

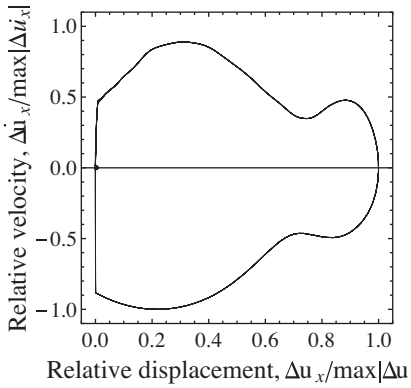

Fig. 5. Phase plane portrait of the relative axial motion among the free ends of the crack. Excitation frequency: $f = 10$ Hz.

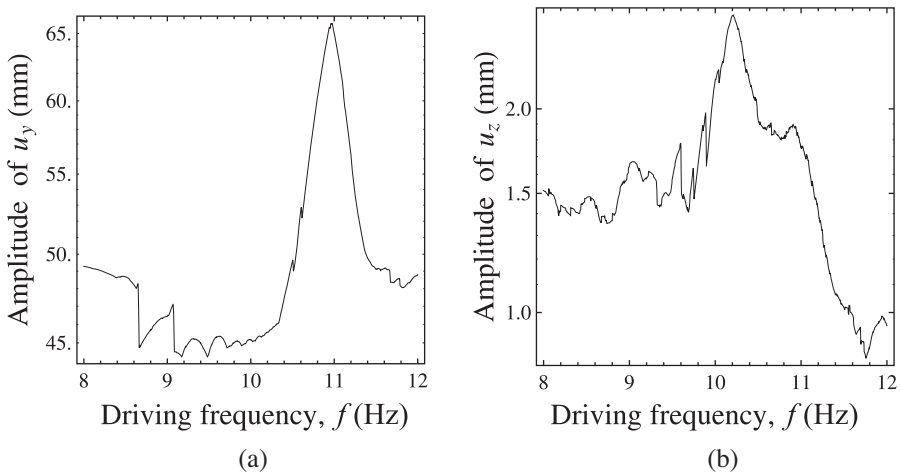

Fig. 6. Amplitude vs. driving frequency for displacements (a) u_y ($\tau_0 = 0.75T_f$) and (b) u_z ($\tau_0 = 0.75T_f$). Time discarded to reach steady state: 2.6 s.

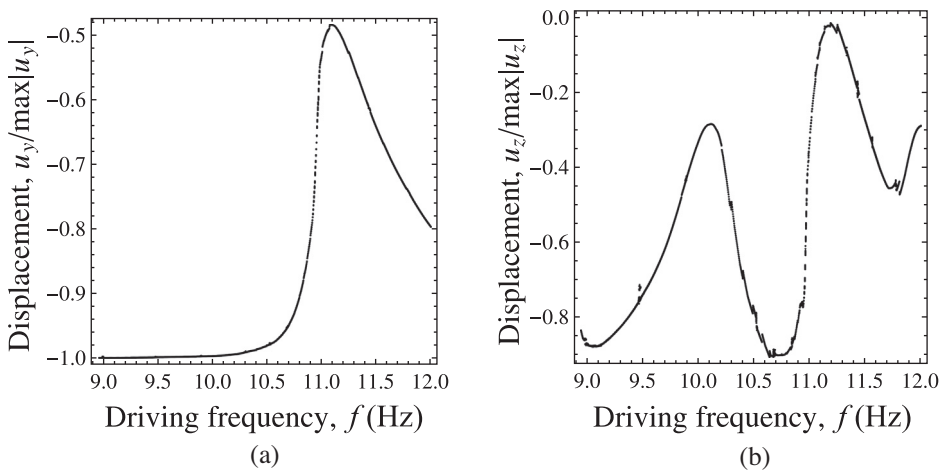

Fig. 7. Bifurcation diagram of displacements (a) u_y ($\tau_0 = 0.75T_f$) and (b) u_z ($\tau_0 = 0.75T_f$). Time discarded to reach steady state: 2.6 s.

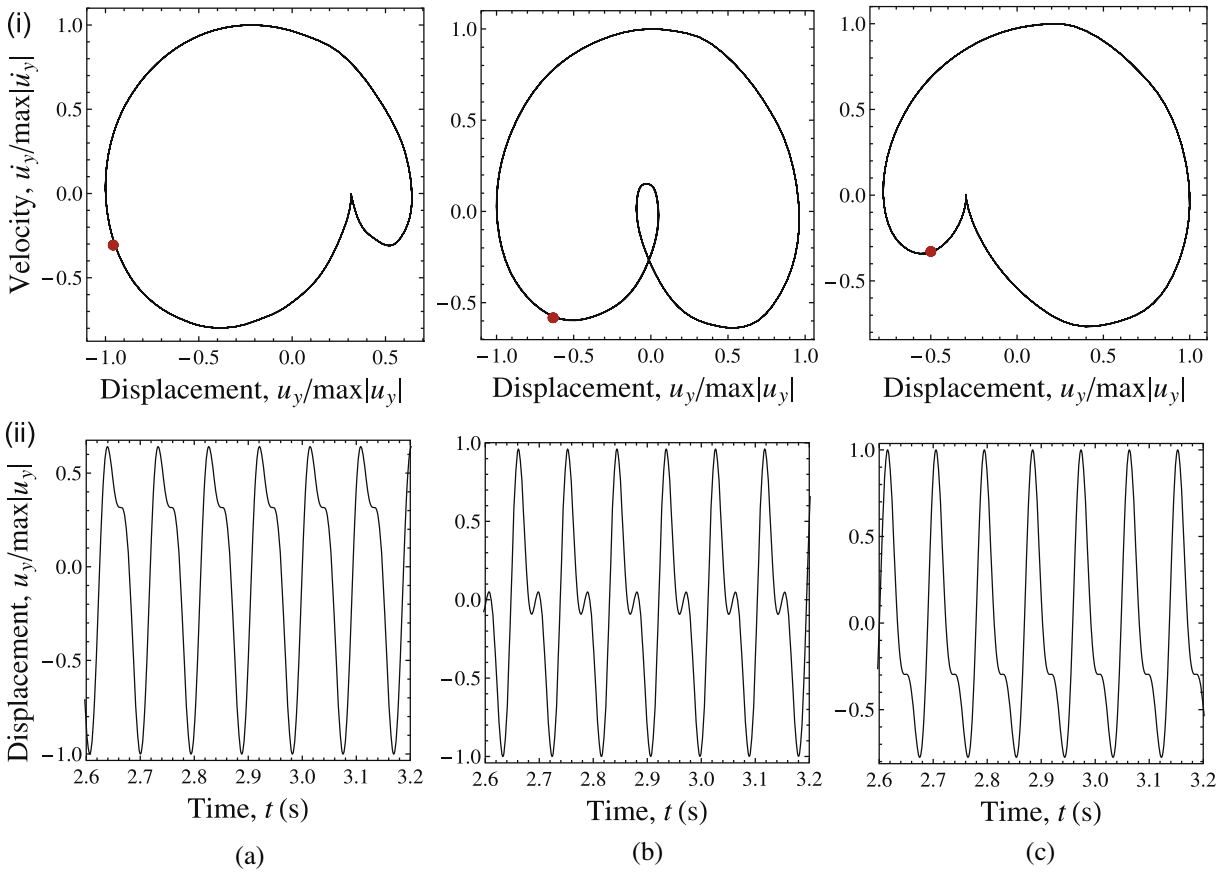

Fig. 8. (i) Orbit plots and Poincaré maps (points in red) for displacement u_y and (ii) associated time histories of motion. Excitation frequency: (a) $f = 10.66$ Hz, (b) $f = 10.96$ Hz, (c) $f = 11.17$ Hz. $\tau_0 = 0.75T_f$. (For interpretation of the references to colour in this figure legend, the reader is referred to the web version of this article.)

can result in significant discrepancies in simulated time domain records. Hence, we consider the result of the comparison as highly satisfactory. However, laboratory experiments must be performed in order to confirm the closure hypotheses of both models. Besides the results of Fig. 4, other comparisons were performed yielding similar results.

The impulsive behavior of breathing is an event which can be observed within the shell model. Fig. 5 shows the phase plane portrait of the relative axial motion among the free ends of the crack. An abrupt change in relative velocity is observed at the moment of closure, which evidences a "quasi-impulsive" behavior, in concordance with the results in Ref. [36] for Euler–Bernoulli beams.

Calculations were performed employing a regular desktop PC. It is worth noting that the beam model takes around one hundred seconds for the simulation of three seconds (this varies with the driving frequency, since the amount of calculations per loading period is fixed). Meanwhile, the shell model requires about two days of computing, for an equivalent simulation. This feature clearly shows the importance of simplified models in the field of structural health monitoring, where calculations must be performed in real time.

4.3. Analysis of topological stability

Using the driving frequency as a parameter, the topological stability of the system is studied. Amplitude–Frequency graphics are observed and then bifurcation diagrams are constructed from Poincaré maps. These maps are obtained by using the sampling rule $t_n = T_f + \tau_0$, where T_f is the period of the driving motion and τ_0 is a constant arbitrarily chosen in order to improve visualization [39].

The study focuses mainly on the excitation of harmonic resonances, which is a common feature of non-linear systems. As the system under study is similar to a bilinear oscillator, these harmonics are located approximately at multiples and sub-multiples of each bilinear frequency, given by:

$$\varpi_B = 2\varpi_0\varpi_C/(\varpi_0 + \varpi_C), \tag{25}$$

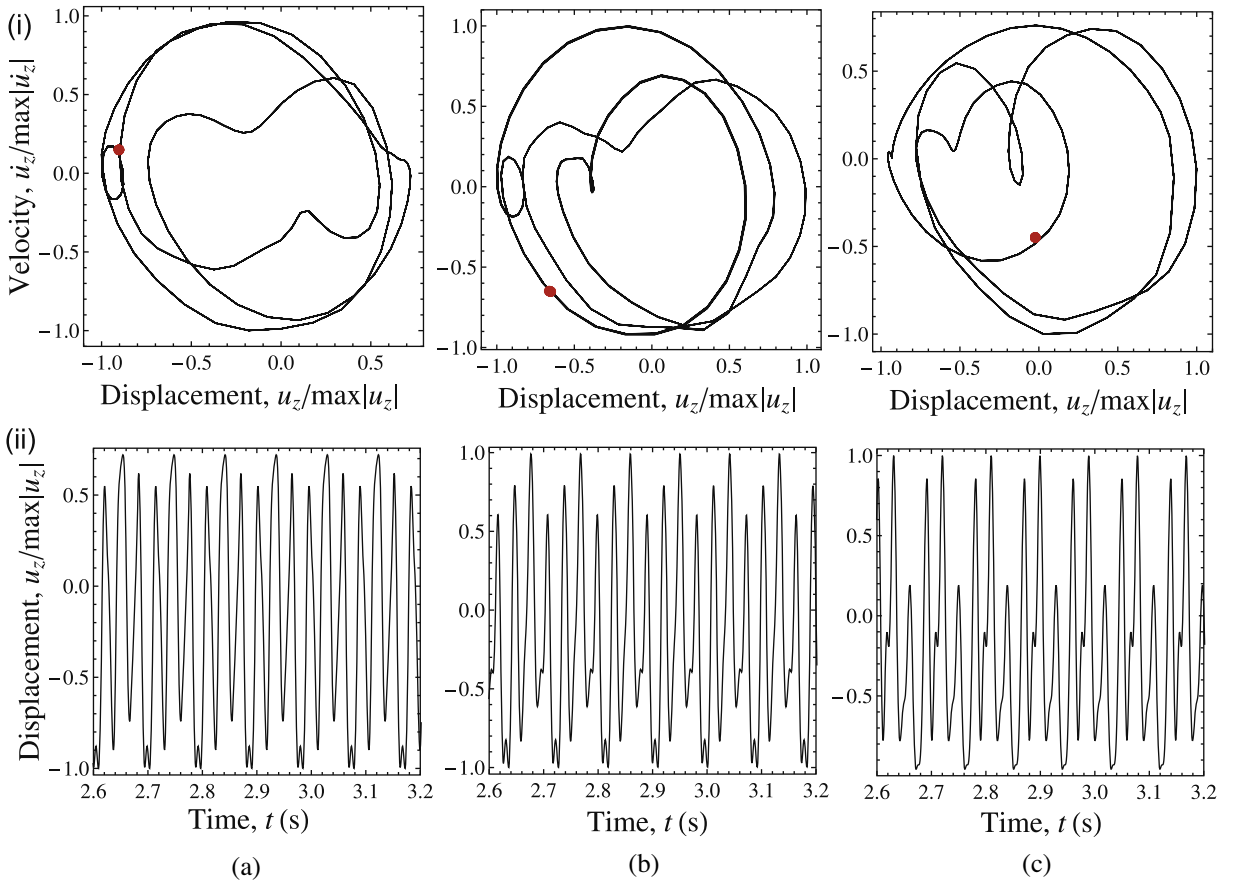

Fig. 9. (i) Orbit plots and Poincaré maps (points in red) for displacement u_z and (ii) associated time histories of motion. Excitation frequency: (a) $f = 10.66$ Hz, (b) $f = 10.96$ Hz, (c) $f = 11.17$ Hz. $\tau_0 = 0.75T_f$. (For interpretation of the references to color in this figure legend, the reader is referred to the web version of this article.)

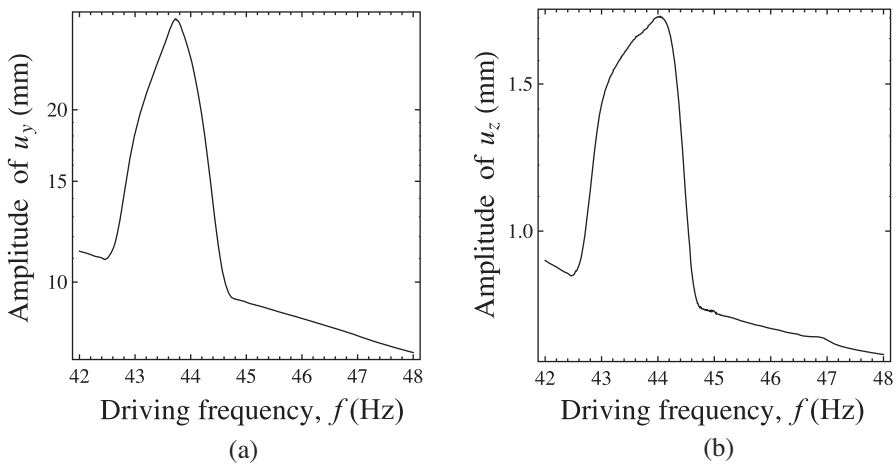

Fig. 10. Amplitude vs. driving frequency for displacements (a) u_y ($\tau_0 = 0.5T_f$) and (b) u_z ($\tau_0 = 0$). Time discarded to reach steady state: 2.5 s.

where ϖ_0 and ϖ_C are generic natural frequencies of the two sub-models: intact beam and open crack, respectively [23,36]. From (25) the first four bilinear frequencies expressed in Hz, $f_B = \varpi_B/(2\pi)$, of the system under study are calculated to give: 22.09 Hz, 30.77 Hz, 72.48 Hz and 131.33 Hz.

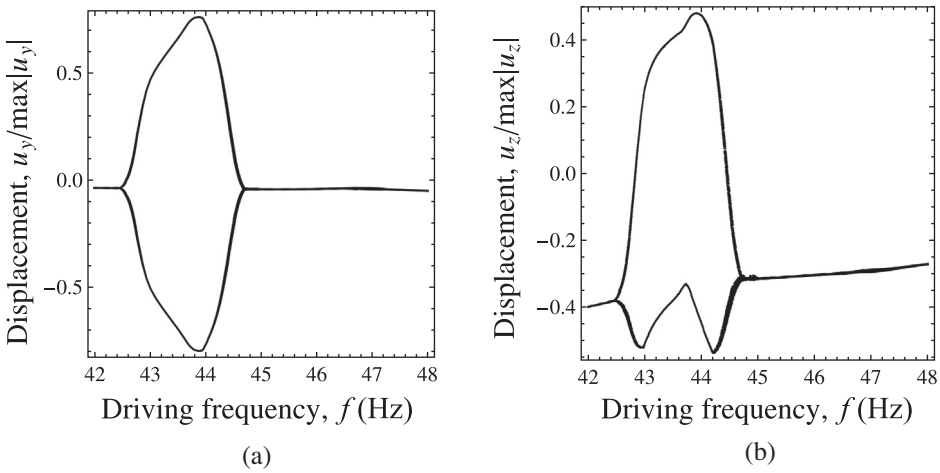

Fig. 11. Bifurcation diagram of displacements (a) u_y ($\tau_0 = 0.5T_f$) and (b) u_z ($\tau_0 = 0$). Time discarded to reach steady state: 2.5 s.

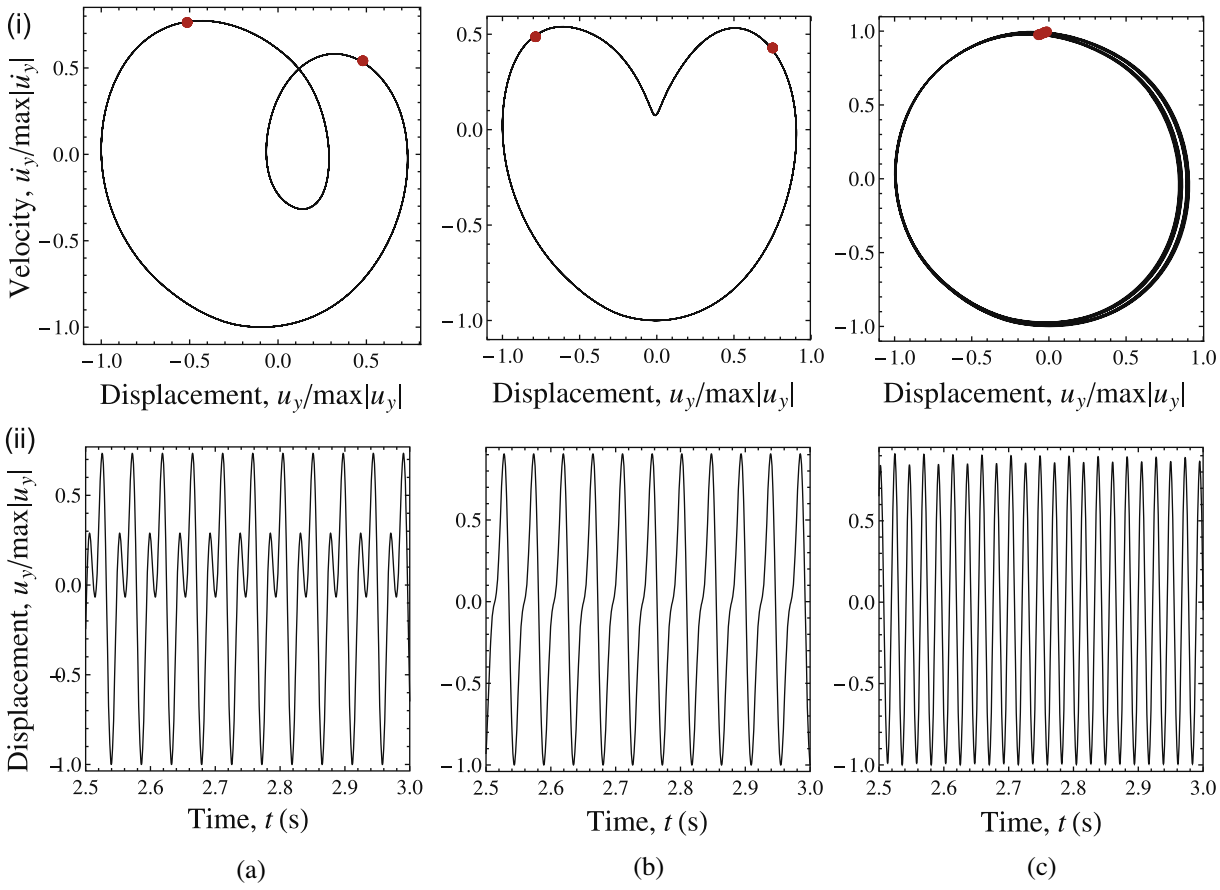

Fig. 12. (i) Orbit plots and Poincaré maps (points in red) for displacement u_y and (ii) associated time histories of motion. Excitation frequency: (a) $f = 43.02$ Hz, (b) $f = 43.77$ Hz, (c) $f = 44.66$ Hz. $\tau_0 = 0.5T_f$. (For interpretation of the references to color in this figure legend, the reader is referred to the web version of this article.)

First we study the response over a driving frequency range of 9–12 Hz (Figs. 6–9). Displacements u_y and u_z of the point P_f are obtained by solving the equations of motion with increments of 0.0025 Hz. For the main displacement (u_y), Fig. 6a shows a pronounced peak almost at 11 Hz. This is very close to the sub-harmonic of order 1/2 of the first bilinear resonance,

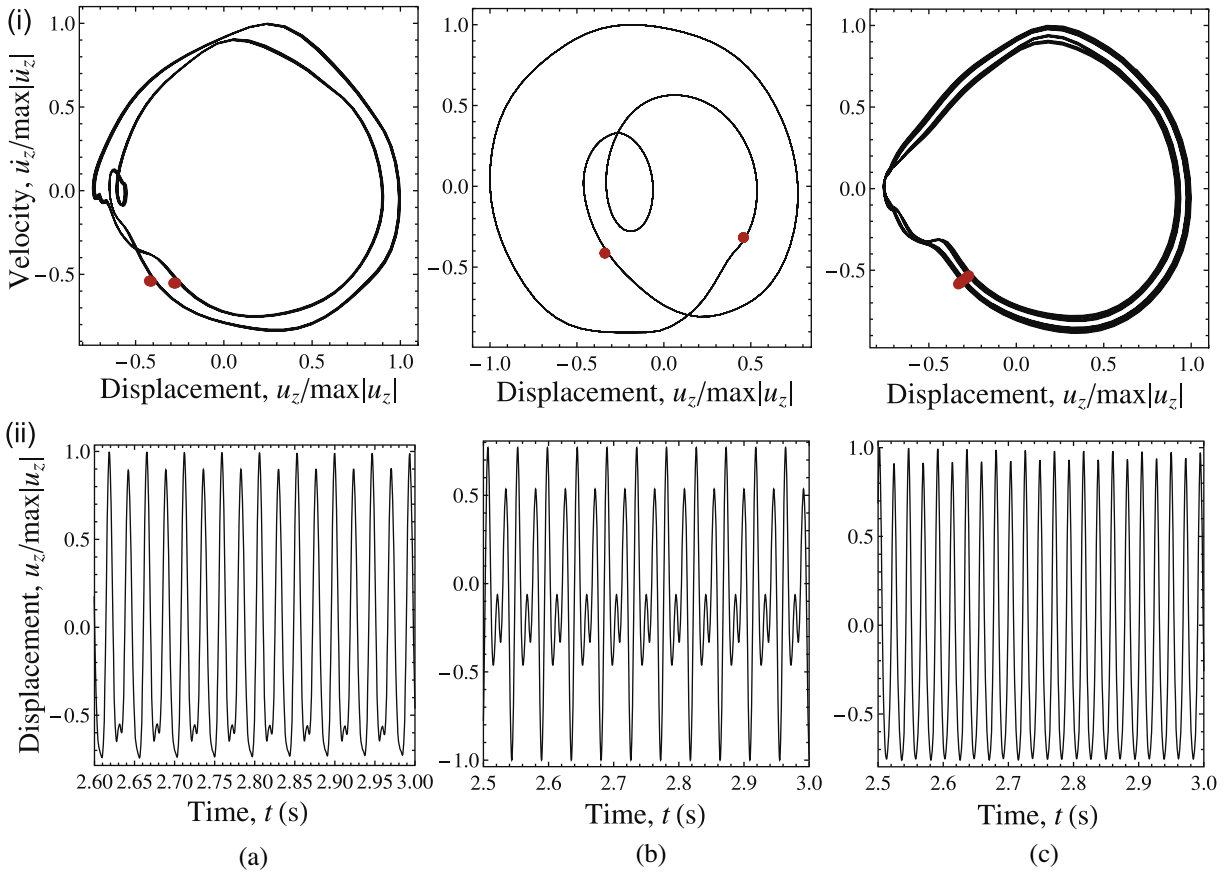

Fig. 13. (i) Orbit plots and Poincaré maps (points in red) for displacement u_z and (ii) associated time histories of motion. Excitation frequency: (a) $f = 42.67$ Hz, (b) $f = 43.77$ Hz, (c) $f = 44.66$ Hz. $\tau_0 = 0$. (For interpretation of the references to color in this figure legend, the reader is referred to the web version of this article.)

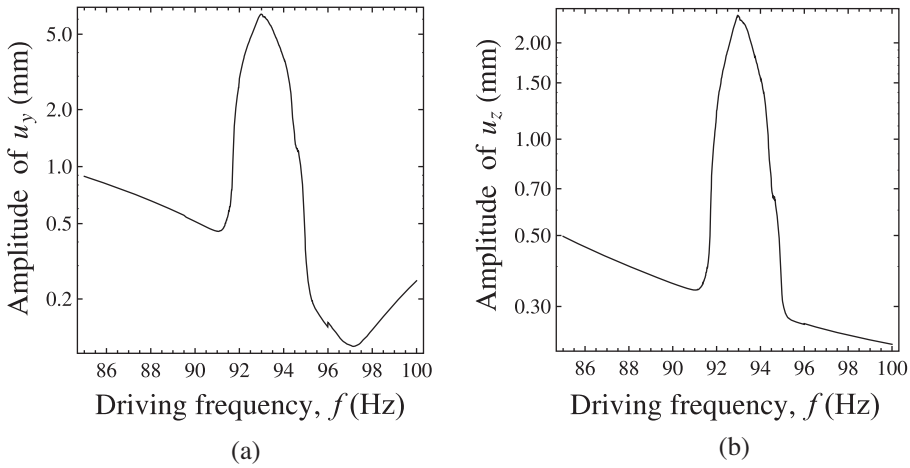

Fig. 14. Amplitude vs. driving frequency for displacements (a) u_y ($\tau_0 = 0$) and (b) u_z ($\tau_0 = 0$). Time discarded to reach steady state: 3.5 s.

corresponding to 11.044 Hz. For the transverse displacement (u_z) Fig. 6b shows a higher amplitude peak at approximately 10.2 Hz; this is next to the sub-harmonic 1/3 of the second bilinear resonance, which is 10.256 Hz. The second resonance has a flexural motion on *xz* plane, with the consequent strong influence in u_z and low influence in u_y. The first resonance is mainly flexural on *xy* plane, hence it has an important influence in u_y.

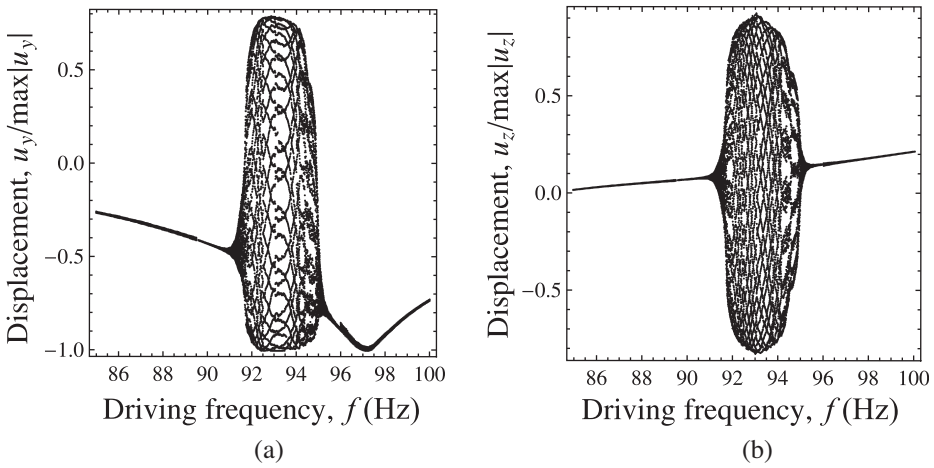

Fig. 15. Bifurcation diagram of displacements (a) u_y ($\tau_0 = 0$) and (b) u_z ($\tau_0 = 0$). Time discarded to reach steady state: 3.5 s.

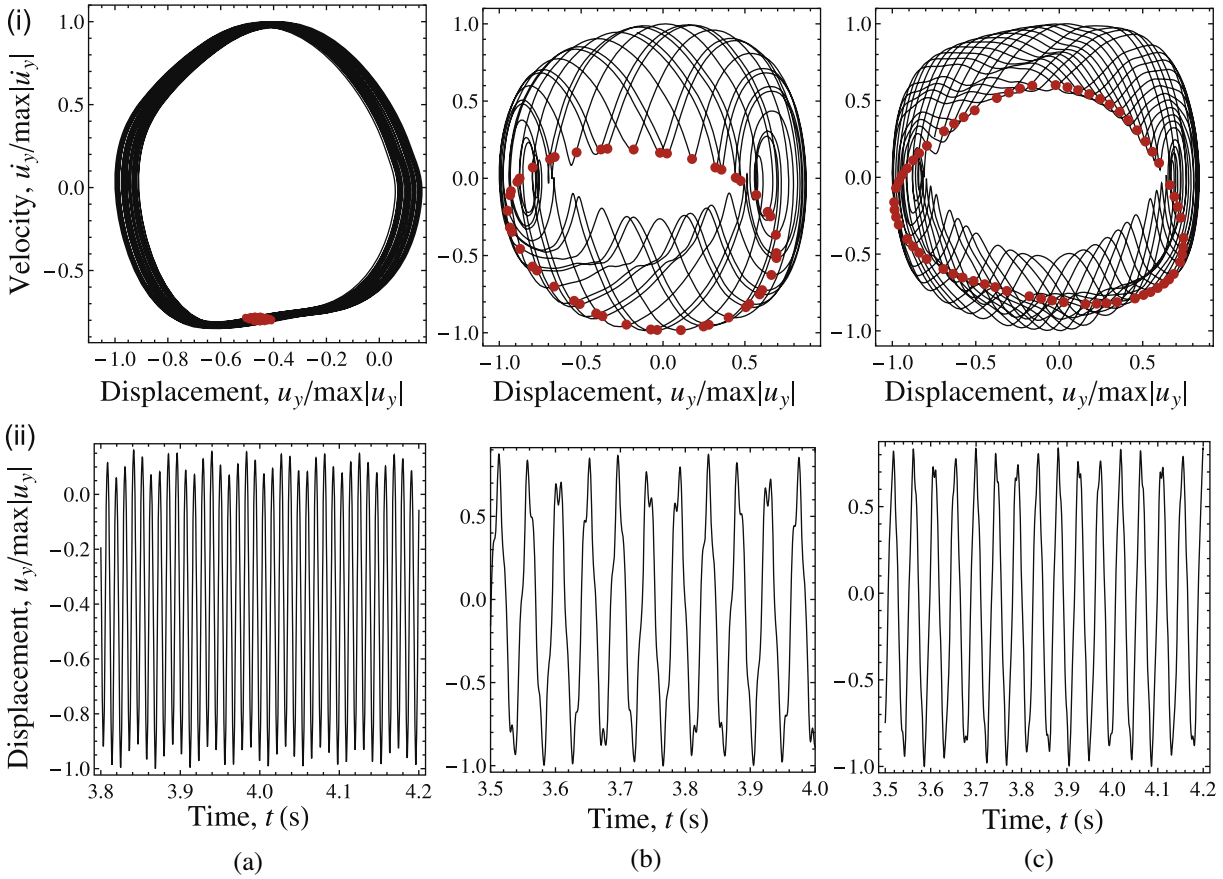

Fig. 16. (i) Orbit plots and Poincaré maps (points in red) for displacement u_y and (ii) associated time histories of motion. Excitation frequency: (a) $f = 91.27$ Hz, (b) $f = 92.30$ Hz, (c) $f = 94.00$ Hz. $\tau_0 = 0$. (For interpretation of the references to color in this figure legend, the reader is referred to the web version of this article.)

As the driving frequency increases, the motion reveals as synchronous with period one in bifurcation diagrams of Fig. 7. For some values of the parameter, orbit plots with superimposed Poincaré maps are presented in Figs. 8 and 9. The perturbation in the curve of Fig. 7a is given by a swirl, but maintaining period one, as can be seen clearly in Poincaré maps of Fig. 8.

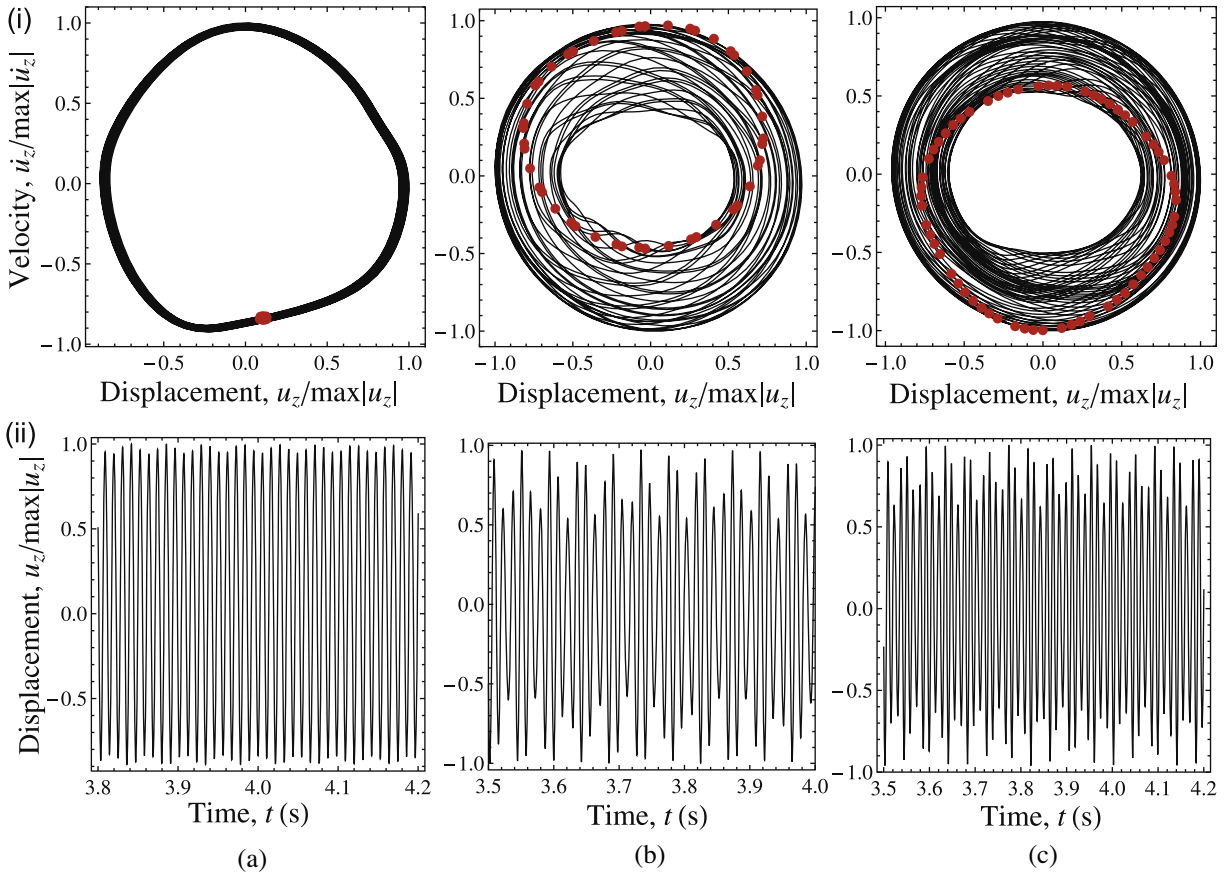

Fig. 17. (i) Orbit plots and Poincaré maps (points in red) for displacement u_z and (ii) associated time histories of motion. Excitation frequency: (a) $f = 91.27$ Hz, (b) $f = 92.30$ Hz, (c) $f = 94.00$ Hz. $\tau_0 = 0$. (For interpretation of the references to color in this figure legend, the reader is referred to the web version of this article.)

This loop initiates at approximately 10.06 Hz and ends at 11.70 Hz, characterizing the strong sub-harmonic behavior [58] associated to the crack closing event. This 'signature' of the breathing crack is evidenced as a perturbation in time histories of Fig. 8. For Euler–Bernoulli beams, this was shown experimentally by Prime and Shevitz [59].

Some minor perturbations are present in the response curve of u_z, as can be seen in the bifurcation diagram of Fig. 7b. These correspond to instabilities which happen within a narrow range of the parameter. In practical terms, the period of the response do not change. This is shown in Fig. 9, as Poincaré maps give a point denoting period one. Orbits present many loops due to the important torsional contribution to displacement u_z.

Results in Figs. 10–13 are employed to study the response over the excitation range 42–48 Hz. Amplitude–Frequency graphics of Fig. 10, obtained by solving with increments of 0.005 Hz, reveal amplitude peaks in the region of 44 Hz. This is approximately twice the first bilinear resonance, i.e. 44.18 Hz. This is a super-harmonic resonance which is accompanied by period doubling, as evidenced by the bifurcation diagrams of Fig. 11 and Poincaré maps of Figs. 12 and 13. The motion bifurcates from period one to period two when the driving frequency reaches 42.47 Hz and then returns to period one at 44.75 Hz.

Finally, we study the response in the neighborhood of super-harmonic 3/1 of the second bilinear frequency, which is located at 92.31 Hz. Amplitude peaks are located at a frequency slightly higher, 93 Hz (refer to Fig. 14), the system maintaining its analogy with the bilinear oscillator. Equations of motion are solved in this case for the range 85–100 Hz, with increments of 0.01 Hz. As can be seen in bifurcation diagrams of Fig. 15, the vibrating beam enters into an intricate motion at approximately 91.2 Hz. This motion results to be quasi-periodic as we observe the associated Poincaré maps of Figs. 16(i)–17(i). Quasi-periodicity is reached directly from period one, as can be seen in Figs. 16a(i) and 17a(i) which represent the onset of the quasi-periodic motion. Poincaré maps give in these cases an 'elliptic point' as transition among period one (point) and quasi-period motion (elliptic orbit). The motion leaves quasi-periodic motion at approximately 95.1 Hz. We observe, within the range of quasi-periodicity, that the characteristic toroidal structure is never broken and hence chaos is not reached. Quasi-periodicity appears to be a not so uncommon phenomenon, as is also observed in other harmonic resonances.

5. Conclusions

In this article, we introduce a refined one-dimensional model to study the dynamics of thin-walled beams with breathing cracks. By virtue of its combination of accuracy and simplicity, this model represents an interesting tool with potential applications to damage identification in slender structures. The breathing effect is modeled with the classic bilinear stiffness, employing the relative axial displacements of the nodes of a cracked finite element as closure index. Implementation is performed during the integration of the equations of motion, through a simple adaptation of the Newmark scheme for linear systems.

Using the driving frequency as a parameter, the non-linear features derived from the breathing effect are studied in a cantilever beam with a crack at one of its flanges. Even with a simple sinusoidal excitation, a variety of topological changes are observed in the vibration motion. These changes are observed at multiples and sub-multiples of the bilinear resonances, showing the similarity of the system under study with a bilinear oscillator. Period doubling and quasi-periodic motion are evidenced by using bifurcation diagrams and Poincaré maps. Although quasi-periodicity can be a route to chaos, we observe in this case that the characteristic toroidal structure is never broken and hence chaos is not reached.

Although model accuracy is tested against a higher hierarchy model, numerical studies presented must be compared with experimental results in order to perform a stronger validation.

Acknowledgments

The authors would like to thank the support of CONICET and Secretaría de Ciencia y Tecnología of Universidad Tecnológica Nacional. The present article is part of the doctoral thesis by Franco Dotti, under the direction of Víctor Cortínez and Marcelo Piovan, at the Department of Engineering of Universidad Nacional del Sur.

References

[1] E.P. Carden, P. Fanning, Vibration based condition monitoring: a review, Struct. Health Monit. 3 (4) (2004) 355–377.
[2] H. Sohn, C.R. Farrar, F.M. Hemez, D.D. Shunk, D.W. Stinemates, B.R. Nadler, J.J. Czarnecki, A review of structural health monitoring literature: 1996–2001, Los Alamos Report LA-13976-MS, 2004.
[3] D. Balageas, C.P. Fritzen, A. Güemes, Structural Health Monitoring, ISTE Ltd, London, 2006.
[4] U. Andreaus, P. Baragatti, Cracked beam identification by numerically analysing the nonlinear behaviour of the harmonically forced response, J. Sound Vib. 330 (4) (2011) 721–742.
[5] S. Christides, A.D. Barr, One-dimensional theory of cracked Bernoulli–Euler beams, Int. J. Mech. Sci. 26 (11–12) (1984) 639–648.
[6] S.L. Tsyfansky, V.I. Beresnevich, Detection of fatigue cracks in flexible geometrically non-linear bars by vibration monitoring, J. Sound Vib. 213 (1) (1998) 159–168.
[7] T.G. Chondros, A.D. Dimarogonas, Vibration of a beam with a breathing crack, J. Sound Vib. 239 (1) (2001) 57–67.
[8] M.B. Rosales, C.P. Filipich, F.S. Buezas, Crack detection in beam-like structures, Eng. Struct. 31 (2009) 2257–2264.
[9] S. Caddemi, I. Calió, M. Marletta, The non-linear dynamic response of the Euler–Bernoulli beam with an arbitrary number of switching cracks, Int. J. Non-Linear Mech. 45 (2010) 714–726.
[10] M. Krawczuk, Coupled longitudinal and bending forced vibration of Timoshenko cantilever beam with a closing crack, J. Theor. Appl. Mech. 32 (2) (1994) 463–482.
[11] J.A. Loya, L. Rubio, J. Fernández-Sáez, Natural frequencies for bending vibrations of Timoshenko cracked beams, J. Sound Vib. 290 (3–5) (2006) 640–653.
[12] A. Ariaei, S. Ziaei-Rad, M. Ghayour, Repair of a cracked Timoshenko beam subjected to a moving mass using piezoelectric patches, Int. J. Mech. Sci. 52 (2010) 1074–1091.
[13] K. Torabi, J. Nafar Dastgerdi, An analytical method for free vibration analysis of Timoshenko beam theory applied to cracked nanobeams using a nonlocal elasticity model, Thin Solid Films 520 (2012) 6595–6602.
[14] V.Z. Vlasov, Thin walled elastic beams, Israel Program for Scientific Translation, Jerusalem, 1961.
[15] A. Gjelsvik, Theory of Thin Walled Beams, John Wiley & Sons, New York, 1981.
[16] V.H. Cortínez, R.E. Rossi, Dinámica de vigas de sección abierta de pared delgada deformables por corte sujetas a un estado inicial de tensiones, Rev. Int. Metod Numer. 14 (1998) 293–316.
[17] V.H. Cortínez, M.T. Piovan, Vibration and buckling of composite thin-walled beams with shear deformability, J. Sound Vib. 258 (4) (2002) 701–723.
[18] M.T. Piovan, V.H. Cortínez, R.E. Rossi, Out-of-plane vibrations of shear deformable continuous horizontally curved thin-walled beams, J. Sound Vib. 237 (1) (2000) 101–118.
[19] S.P. Machado, V.H. Cortínez, Non-linear model for stability of thin-walled composite beams with shear deformation, Thin Wall. Struct. 43 (2005) 1615–1645.
[20] M.T. Piovan, V.H. Cortínez, Mechanics of thin-walled curved beams made of composite materials, allowing for shear deformability, Thin Wall. Struct. 45 (2007) 759–789.
[21] V.H. Cortínez, F.E. Dotti, Un modelo numérico para la dinámica de vigas de pared delgada fracturadas por fatiga: Aplicación a la identificación de daños, Mecánica Computacional 29 (2010) 431–448.
[22] S.P. Machado, C.M. Saravia, F.E. Dotti, Non-linear oscillations of a thin-walled composite beam with shear deformation, Appl. Math. Model. 38 (4) (2013) 1523–1533.
[23] J.A. Brandon, Some insights into the dynamics of defective structures, Proc. Inst. Mech. Eng. 212C (1998) 441–454.
[24] M.I. Friswell, Damage identification using inverse methods, Philos. Trans. R. Soc. A. 365 (2007) 393–410.
[25] J.E. Penny, M.I. Friswell, Crack modeling for structural health monitoring, Struct. Health Monit. 1 (2) (2002) 139–148.
[26] U. Andreaus, P. Casini, F. Vestroni, Frequency reduction in elastic beams due to a stable crack: numerical results compared with measured test data, Eng. Trans. 51 (1) (2003) 1–16.
[27] U. Andreaus, P. Baragatti, Fatigue crack growth, free vibrations and breathing crack detection of aluminium alloy and steel beams, J. Strain Anal. Eng. 44 (7) (2009) 595–608.
[28] J.A. Brandon, O.N. Abraham, Counter-intuitive quasi-periodic motion in the autonomous vibration of cracked Timoshenko beams, J. Sound Vib. 185 (3) (1995) 415–430.
[29] N. Pugno, C. Surace, R. Ruotolo, Evaluation of the non-linear dynamic response to harmonic excitation of a beam with several breathing cracks, J. Sound Vib. 235 (5) (2000) 749–762.

[30] P.N. Saavedra, L.A. Cuitiño, Crack detection and vibration behavior of cracked beams, Comput. Struct. 79 (2001) 1451–1459.
[31] S.M. Cheng, X.J. Wu, W. Wallace, Vibrational response of a beam with a breathing crack, J. Sound Vib. 225 (1) (1999) 201–208.
[32] A.K. Darpe, K. Gupta, A. Chawla, Coupled bending, longitudinal and torsional vibrations of a cracked rotor, J. Sound Vib. 269 (2004) 33–60.
[33] T.H. Patel, A.K. Darpe, Influence of crack breathing model on nonlinear dynamics of a cracked rotor, J. Sound Vib. 311 (2008) 953–972.
[34] S. El Arem, Q.S. Nguyen, Nonlinear dynamics of a rotating shaft with a breathing crack, Ann. Solid Struct. Mech. 3 (2012) 1–14.
[35] M. Kisa, J.A. Brandon, The effects of closure of cracks on the dynamics of a cracked cantilever beam, J. Sound Vib. 238 (1) (2000) 1–18.
[36] U. Andreaus, P. Casini, F. Vestroni, Non-linear dynamics of a cracked cantilever beam under harmonic excitation, Int. J. Non-Linear Mech. 42 (2007) 566–575.
[37] F.S. Buezas, M.B. Rosales, C.P. Filipich, Damage detection with genetic algorithms taking into account a crack contact model, Eng. Fract. Mech. 78 (2011) 695–712.
[38] U. Andreaus, P. Baragatti, Experimental damage detection of cracked beams by using nonlinear characteristics of forced response, Mech. Syst. Signal Process. 31 (8) (2012) 382–404.
[39] F.C. Moon, Chaotic Vibrations: An Introduction for Applied Scientists and Engineers, John Wiley & Sons, New Jersey, 2004.
[40] Y.J. Xie, H. Xu, P.N. Li, Crack mouth energy-release rate and its application, Theor. Appl. Fract. Mech. 29 (3) (1998) 195–203.
[41] Y.J. Xie, X.H. Wang, Y.C. Lin, Stress intensity factors for cracked rectangular cross-section thin-walled tubes, Eng. Fract. Mech. 71 (2004) 1501–1513.
[42] V.H. Cortínez, F.E. Dotti, Mode I stress intensity factor for cracked thin-walled open beams, Eng. Fract. Mech. 110 (2013) 249–257.
[43] G. Hermann, H. Sosa, On bars with cracks, Eng. Fract. Mech. 24 (1986) 889–894.
[44] Z.P. Bazant, Justification and improvement of Kienzler and Hermann estimate of stress intensity factors of cracked beams, Eng. Fract. Mech. 36 (1990) 523–525.
[45] J.R. Rice, A path independent integral and the approximate analysis of strain concentration by notches and cracks, J. Appl. Mech. 35 (1968) 379–386.
[46] R. Clough, J. Penzien, Dynamics of Structures, Computers & Structures, Berkeley, 2003.
[47] A.P. Bovsunovsky, The mechanisms of energy dissipation in the non-propagating fatigue cracks in metallic materials, Eng. Fract. Mech. 71 (2004) 2271–2281.
[48] A. Rytter, R. Brincker, P.H. Kirkegaard, An experimental study of the modal parameters of a cantilever, Fracture & Dynamics, Paper 37, Department of Building Technology and Structural Engineering, Aalborg University, 1992.
[49] K. Jendoubi, N. Ranganathan, N. Merah, Effect of thickness on elasto-plastic deformation and hysteresis energy dissipated at crack tip, J. Test. Eval. 19 (3) (1991) 201–209.
[50] A.P. Bovsunovskii, Vibrations of a nonlinear mechanical system simulating a cracked body, Strength Mater. 33 (4) (2001) 370–379.
[51] R. Gasch, A survey of the dynamic behaviour of a simple rotating shaft with a transverse crack, J. Sound Vib. 160 (2) (1993) 313–332.
[52] J.N. Sundermeyer, R.L. Weaver, On crack identification and characterization in a beam by non-linear vibration analysis, J. Sound Vib. 183 (5) (1995) 857–871.
[53] K.-J. Bathe, Finite Element Procedures, Prentice Hall, New Jersey, 1996.
[54] ABAQUS/Analysis User's Manual, vol. V, v6.7. Dassault Systèmes, 2007.
[55] ABAQUS/Analysis User's Manual, vol. II, v6.7. Dassault Systèmes, 2007.
[56] J.A. Brandon, M.H. Mathias, Complex oscillatory behaviour in a cracked beam under sinusoidal excitation, J. Sound Vib. 186 (2) (1995) 350–354.
[57] O.N.L. Abraham, J.A. Brandon, A piece-wise linear model for the modeling of a breathing crack, in: Fifth International Conference on Experimental and Numerical Methods in Structural Dynamics 1597–1609, Leuven, Belgium, September 1988.
[58] M.C. Teich, S.E. Keilson, S.M. Khanna, Models of nonlinear vibration. II Oscillator with bilinear stiffness, Acta Otolaryngol. 467 (1989) 249–256.
[59] M.B. Prime, D.W. Shevitz, Linear and nonlinear methods for detecting cracks in beams, in: Proceedings of the XIV International Modal Analysis Conference (IMAC), 1437–1443, Dearborn, USA, February 1996.